IOP Conf. Series: Materials Science and Engineering **409** (2018) 012012 doi:10.1088/1757-899X/409/1/012012

A Comparative Study of Visible Raman Scattering of Ceria Prepared by Sol-gel and Hydrothermal Techniques with Gold Nanoparticles

Muhammad Nur Syafi'ie Md Idris[1,*], Hai-Pang Chiang[2,3], Noormariah Muslim[1], Yuan-Fong Chou Chau[1], Abdul Hanif Mahadi[1], Nyuk Yoong Voo[1], and Chee Ming Lim[1]

[1]Centre for Advanced Material and Energy Sciences, Universiti Brunei Darussalam, Jalan Tungku Link, Gadong, BE 1410, Brunei Darussalam
[2]Institute of Optoelectronic Sciences, National Taiwan Ocean University, No. 2 Pei-Ning Rd., 202, Keelung, Taiwan
[3]Institute of Physics, Academia Silica, Taipei 11529, Taiwan

*E-mail: 14h8703@ubd.edu.bn / nursyafiee@hotmail.com

Abstract. Nano-structured ceria was synthesized by using sol-gel and hydrothermal techniques. Prior to measurements by Raman spectroscopy, the prepared ceria was dispersed onto glass substrates by spin-coating, and this was followed by the deposition of gold nano-particles onto the surface of the ceria by direct current magnetron sputtering. The F_{2g} Raman peak, oxygen vacancy and longitudinal optical modes of ceria were successfully observed with visible Raman laser excitation wavelength of 532 nm at non-resonance Raman conditions. The surface oxygen adsorption on ceria surface was also detected. The F_{2g} Raman peaks of ceria for all of the samples were red-shifted because of the nano-crystalline structure and strain effect on the samples. In the case of the hydrothermally processed gold coated ceria, the F_{2g} Raman peak was further red-shifted to 451 cm^{-1} because of temperature effect and anharmonicity, and the peak intensity was also found to be enhanced by at least one order of magnitude (x13). This increase in peak intensity was attributed to the electrical field enhancement via localized surface plasmon resonance of the gold nano-particles.

1. Introduction

Cerium dioxide (ceria, CeO_2) has been widely known to have variations of defects in its lattice structure. The energy calculations show that these defects can be allocated into four particular groups and these are; (a) oxygen vacancy site, (b) anion Frenkel pairs, (c) interstitial sites, and (d) Schottky disorders [1-3]. Amongst these defects, the most attractive to our work is the oxygen vacancy site (i.e. one of the lattice position experience an oxygen atom lost) which are essential for oxygen storage [4, 5], oxygen reduction[6], water splitting [7-10], thermal conductivity [11] and carbon monoxide oxidation [12, 13] applications.

UV Raman spectroscopy has been extensively used to identify oxygen vacancy site in ceria because of the strong absorption of UV light and the effect of Raman resonance which provides high probing sensitivity [14-16]. The UV excitation activates overtone bands of second-order longitudinal optical (2LO) mode of ceria which are caused by multi-phonon excitation at resonance. The

observations of oxygen vacancy and 2LO mode are rarely reported in visible Raman spectroscopy because of the weak absorption and non-resonance Raman conditions.

However, in this study, by dispersing ceria on glass substrates, prominent Raman spectra of ceria oxygen vacancy and 2LO were observed. In addition, ceria was synthesized by using two different techniques, i.e. sol-gel (SG) and hydrothermal (HT) for comparison purposes. Besides, in order to study the effect of gold on the Raman spectra of ceria, gold nano-particles (NPs) were deposited on top of ceria by sputtering method. A finite element method was performed to demonstrate the electrical field intensity distribution of ceria with gold NPs. Crystal structure, surface morphology, and optical properties of the samples were also investigated.

2. Experimental Section

2.1. Preparation of Ceria by Sol-Gel (SG) Method

Cerium (III) nitrate hexahydrate ($Ce(NO_3)_3.6H_2O$, 98%) and ethanol (C_2H_5OH, absolute, 99.9%) from Merck Millipore were used in the sol-gel method for the synthesizations of ceria. Initially, an aqueous solution was prepared by dissolving 5 g of $Ce(NO_3)_3.6H_2O$ in 10 ml of ethanol inside a beaker. Then, the beaker was covered with aluminium foil. The solution was continuously stirred for 20 h in ambient atmosphere. A small portion of the solution was dropped onto a flat glass substrate and heated in air at 100 °C for 1 h and 150 °C for 20 min on a hot plate. As a result, chalky foam was produced which was then dried at 150 °C for 1 h and 250 °C for 10 min. In order to obtain the powder, the dried foam was crushed by using an agate mortar and pestle. Finally, the powder was calcined at 500 °C for 1 h (2 °C/min). The powder was labelled as ceria-SG.

2.2. Preparation of Ceria by Hydrothermal (HT) Method

In this method, cerium (III) nitrate hexahydrate ($Ce(NO_3)_3.6H_2O$, 98%) and sodium hydroxide (NaOH, 93.0%, Merck Millipore) were used for the ceria production. At first, 7.282 g of NaOH was dissolved in 30 ml of distilled water. Then, 0.746 g of $Ce(NO_3)_3.6H_2O$ was added into the solution and stirred for 30 minutes. The solution with the precipitate was then transferred to an autoclave and heat-treated at 100 °C for 24 h. As the autoclave was cooled down to room temperature, the excess solution was poured off to retrieve the solid. It was filtered and washed with distilled water until neutral pH was reached, and finally dried at 100 °C for 24 h. The solid was in the form of powder and labelled as ceria-HT.

2.3. Deposition of Gold NPs onto Ceria Surfaces

The prepared ceria-SG (50 mg) was ultrasonicated in ethanol (5 ml) for 30 min (step 1). The suspension (0.1 ml) was then dropped onto cleaned soda lime glass substrate (step 2) and spin-coated for 1 min at spinning rate of 2000 r.p.m (step 3). The dispersed ceria was left to dry for 1 min (step 4). These steps (2-4) were repeated for 3 times on the same surface. The same procedure was also employed for ceria-HT. All of the dispersed ceria on the glass substrates was dried in an oven at 100 °C for 4 h. Gold was then deposited onto the surface of ceria via direct current (DC) magnetron sputtering technique (SPI Module, Sputter Coater) at DC supply of about 7.0 – 9.0 mA and pressure of 10^{-1} Torr at room temperature with deposition time of 90 s. The samples were named as gold-ceria-SG and gold-ceria-HT, respectively.

2.4. Sample Characterization

X-ray diffraction (XRD-7000, Shimadzu) was used to analyze the crystal structure of the samples with monochromatic high-intensity CuKα (λ=1.54056 Å) radiation operated at 40 kV and 30 mA. The samples were scanned at a rate of 2°/min in the range of 2θ = 10–80° and at incident angle of 1.0°. A JEOL JSM-7610F field emission scanning electron microscopy (FE-SEM) was used to obtain the image of the surface of the sample. The images were captured at magnifications of x50,000 with an accelerating voltage of 5.0 kV and 7.0 kV. The measurements of optical absorbance of the samples

were conducted by using a UV-Vis-NIR spectrophotometer (CARY 5000) in wavelength range of 300 nm to 800 nm. Moreover, a confocal micro-Raman spectrometer (CRM200, WITec) with a semiconductor laser excitation of 532 nm at 30 mW was used to record the Raman spectra of the samples at room temperature. A computational simulation by using finite element method (FEM) was conducted [17-20].

3. Results and Discussion

3.1. XRD and FE-SEM Analysis of Ceria and Gold NPs

The XRD patterns of dispersed ceria coated with gold NPs on glass substrates are presented in Fig.1. All samples indexed to the CeO_2 with cubic fluorite structure, as certified with the standard ICDD: card no. 00-043-1002. The diffraction peaks of ceria at 2θ: 28.6° (111), 32.6° (200), 47.6° (220) and 56.3° (311) were identified for ceria-SG and gold-ceria-SG. In the case of ceria-HT and gold-ceria-HT, the diffraction peaks were at 2θ: 28.6° (111), 32.7° (200), 47.4° (220) and 56.4° (311). The diffraction peaks of gold appeared at 2θ: 37.9° (111), 44.1° (200) and 64.5° (220) for gold-ceria-SG and at 2θ: 38.1° (111) for gold-ceria-HT (standard ICDD: card no. 00-004-0784). Based on Scherrer equation and line broadening, the average crystallite size of ceria for ceria-SG, gold-ceria-SG, ceria-HT and gold-ceria-HT were approximated to be 13.2 nm, 13.5 nm, 12.9 nm and 12.7 nm, respectively. The estimated average crystallite size of gold was 32.3 nm and 64.6 nm for gold-ceria-SG and gold-ceria-HT, respectively.

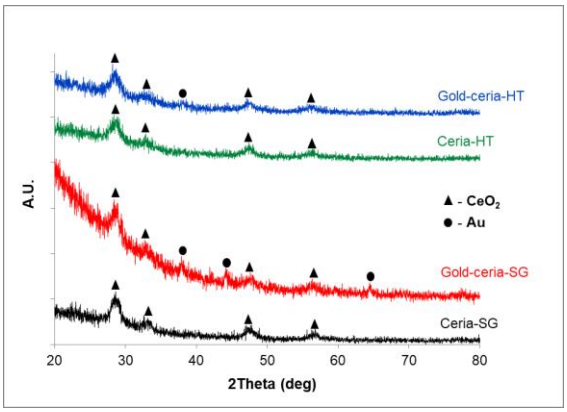

Figure 1. X-Ray Diffraction patterns of: ceria-SG (black); gold-ceria-SG (red); ceria-HT (green); and gold-ceria-HT (blue).

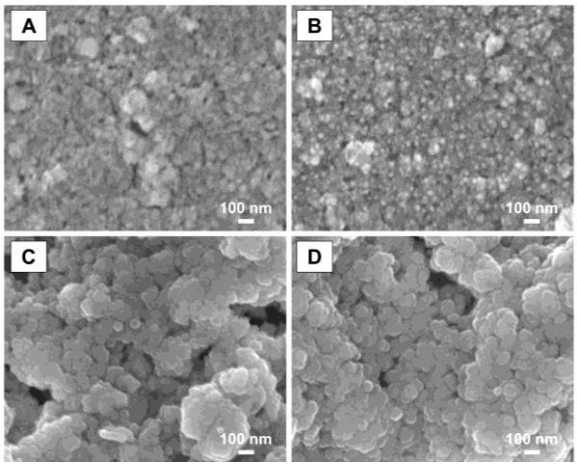

Figure 2. FE-SEM images of: [A] ceria-SG; [B] gold-ceria-SG; [C] ceria-HT; and [D] gold-ceria-HT.

The FE-SEM images of the samples are displayed in Fig.2. The images show the surface morphology of the dispersed ceria. The ceria-SG (Fig.2(A)) has different surface morphology than the ceria-HT (Fig.2(C)). No distinct profile was observed for the surface of ceria-SG, while ceria-HT was found to be in cauliflower-like surface. In general, metal was found to nucleate in the oxygen vacancy sites in fluorite structure [21]. Moreover, high concentration of oxygen vacancies contributes to the high dispersion of gold [22] that leads to the formation of smaller gold NPs. Thus, in this work, the average crystallite size of gold for gold-ceria-SG (32.3 nm) was smaller than that of gold-ceria-HT (64.6 nm).

3.2. UV-Vis Absorbance and Raman Spectra Analysis of Ceria and Gold NPs

The absorption spectra of the samples in the range of 300 nm to 800 nm are presented in Fig.3. Ceria coated with gold NPs showed an increase in the absorption compared to un-coated ceria. Furthermore, the absorption of ceria-SG and gold-ceria-SG (Fig.3(A)) was higher than the ceria-HT and gold-ceria-HT (Fig.3(B)). Despite of the low absorption of ceria-HT, it showed an increase in absorption in the visible range (grey region) due to gold-ceria interactions [23].

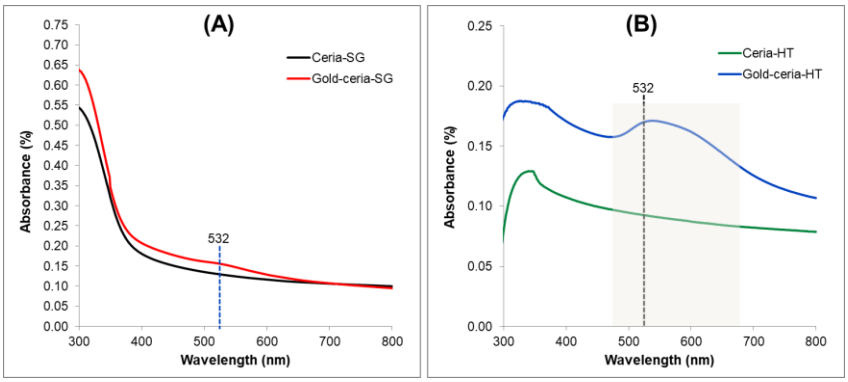

Figure 3. UV-Vis absorption spectra of: (A) ceria-SG (black); gold-ceria-SG (red); and (B) ceria-HT (green); gold-ceria-HT (blue).

Fig.4 shows the Raman spectra of the samples measured at laser excitation wavelength of 532 nm with power of 30 mW. In Fig.4(A), the Raman spectra of ceria-SG showed several Raman peaks centered at 461 cm^{-1}, 558 cm^{-1}, 783 cm^{-1} and 1098 cm^{-1}, whereas peaks for gold-ceria-SG were at 457 cm^{-1}, 557 cm^{-1}, 781 cm^{-1} and 1100 cm^{-1}. These Raman peaks have been corresponded to the first-order F_{2g} Raman mode for cubic ceria [24], oxygen vacancy defects (D) [25], surface oxygen adsorption [15] and second-order longitudinal optical (2LO) mode [14, 26], respectively. In the case of ceria-HT as shown in Fig.4(B), the peaks were at 457 cm^{-1}, 555 cm^{-1}, 785 cm^{-1}, and 1098 cm^{-1}, while peaks for gold-ceria-HT were at 451 cm^{-1}, 567 cm^{-1}, 763 cm^{-1} and 1101 cm^{-1}. In this study, visible Raman laser was used to reveal the oxygen vacancy and 2LO spectra. This could be made possible because of the dispersion of ceria on the glass substrate which increased the exposure of the oxygen vacancy site and allowed the activation of the 2LO Raman mode. Hence, this method could improve the detection sensitivity of visible Raman spectroscopy of ceria.

The F_{2g} Raman peak, full-width half maximum (FWHM), intensity, as well as, the defects (D) peak (oxygen vacancy) of the samples are tabulated in Table 1. In general, the F_{2g} Raman peak of bulk ceria has been reported to be at 464 cm^{-1}[27]. Nonetheless, all of the samples showed a decrease (red-shift) in the F_{2g} Raman peak of ceria. This has been attributed to the nano-structured ceria and strain effects [28]. In addition, the further red-shift of the F_{2g} Raman peak of ceria to 451 cm^{-1} for gold-ceria-HT (Fig.4(B)) was caused by temperature effects and anharmonicity [29], which originated from plasmon heating by localized surface plasmon resonance (LSPR) decay of the gold NPs [30]. Apart from that, there was a significant increase in the intensity of the F_{2g} Raman peak of gold-ceria-HT when

compared to ceria-HT, i.e. from 259 a.u. to 3542 a.u. which was 13 times higher than ceria without gold NPs. The gold NPs amplified the Raman signals as a result of surface-enhanced Raman scattering (SERS) from the LSPR of gold NPs that occurred at the laser excitation wavelength of 532 nm. Furthermore, an increase in the absorption of visible spectra was observed, as shown in the grey region of Fig.3(B), where the Raman laser excitation wavelength of 532 nm was located. In contrast, there was no intensification of the Raman intensity of the F_{2g} Raman peak for gold-ceria-SG. This might be due to the size of the gold NPs which were not favorable for LSPR to occur.

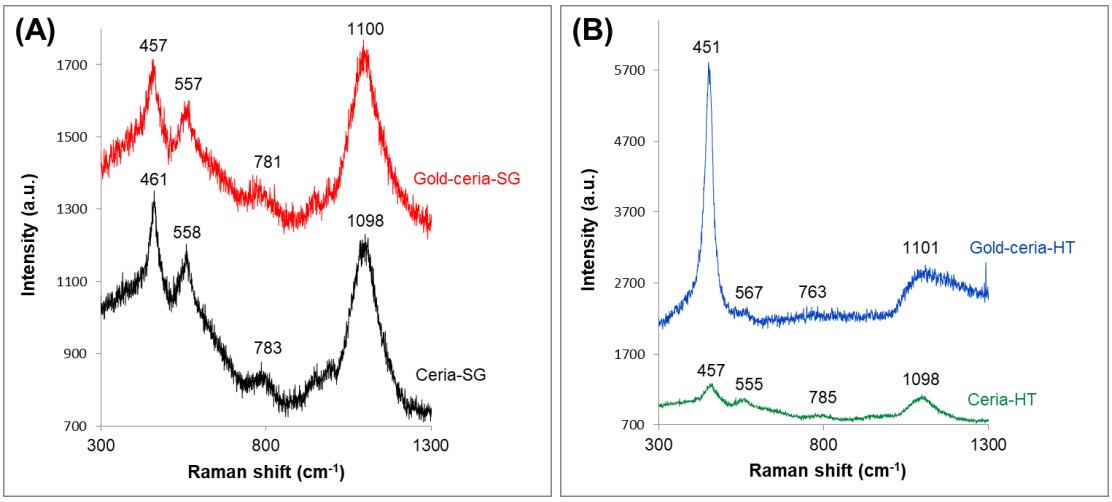

Figure 4. Raman spectra of: (A) ceria-SG (black); gold-ceria-SG (red); and (B) ceria-HT (green); gold-ceria-HT (blue).

Table 1. Average Crystallite Size, F_{2g} Raman Peaks and Intensities, D Raman Peaks and Intensities, and Estimated FWHM Of The Samples.

Sample	CeO_2 Crystallite size (nm)	Au Crystallite size (nm)	F_{2g} Raman Peak (cm^{-1})	F_{2g} FWHM (cm^{-1})	F_{2g} Raman intensity (a.u.)	D Raman Peak (cm^{-1})	D Raman intensity (a.u.)
Ceria [SG]	13.2	-	461	25.3	296	558	188
Gold-ceria [SG]	13.5	32.3	457	36.7	241	557	176
Ceria [HT]	12.9	-	457	36.7	259	555	132
Gold-ceria [HT]	12.7	64.6	451	29.5	3542	567	-

3.3. Finite element method simulation

In order to analyze the existence of the enhanced electrical field (E-field) intensity distributions (Fig.5(A)), and the surface charge densities (Fig.5(B)) contributed by the gold NPs from gold-ceria-SG (32.3 nm) and gold NPs from gold-ceria-HT (64.6 nm) at the excitation wavelength (λ) of 532 nm with x-polarization, computational simulations were performed by using the finite element method (FEM) with perfect matched layers on the top and bottom surface of the unit cell. The imaginary dielectric constant of gold will give a negative damping effect to the LSPR and the gold permittivity data cited in [31] was used. It could be seen that the enhanced E-fields and surface charges could be excited around the gold NPs and the interface between gold NPs and ceria, which is caused by the LSPR effects [18, 32, 33]. Moreover, the E-field enhancement could also be attributed to gap plasmon resonance (GPR) [19, 34, 35]. Note that the different in the charge pair configuration (Fig.5(B)) is due to different resonant mode arising from different incident resonant wavelength. In addition, the E-field intensity distribution obtained from larger gold NPs (Fig.5(A,ii)) was higher than that of the smaller gold NPs (Fig.5.(A,i)). This is because of the existence of more charge pairs and hence their higher

density distribution on the surface of the larger gold NPs (Fig.5(B,ii)). Thus, this E-field enhancement leads to the surface-enhanced Raman scattering (SERS) which is responsible for the intensification of ceria F_{2g} Raman peak of gold-ceria-HT sample.

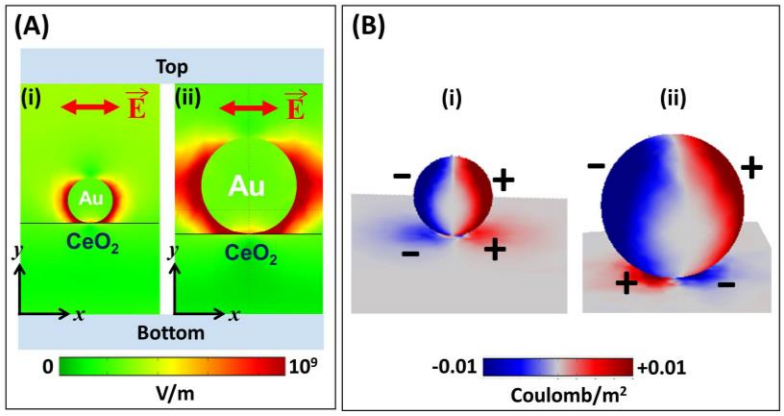

Figure 5. Calculated E-field intensity distributions of gold NPs on ceria for gold-ceria-SG (A,i) and gold-ceria-HT (A,ii); surface charge densities of gold NPs on ceria for gold-ceria-SG (B,i) and gold-ceria-HT (B,ii), excited by an incident light with linearly polarized plane wave (λ= 532 nm).

4. Conclusion

In this study, visible Raman spectroscopy with laser excitation wavelength of 532 nm was demonstrated to detect the F_{2g} Raman peak, oxygen vacancy, oxygen adsorption as well as longitudinal optical mode of ceria prepared by sol-gel and hydrothermal techniques. The dispersion of ceria onto glass substrates assisted in revealing these peaks in non-resonance Raman conditions. Furthermore, the F_{2g} Raman peaks of ceria were red-shifted because of the nano-structured ceria and strain effect. The additional red-shift of ceria prepared by hydrothermal method demonstrated temperature effect and anharmonicity originated from plasmon heating via LSPR decay of gold NPs. Besides, the observation of E-field enhancement attributed to LSPR effect which caused SERS produced a significant amplification of the F_{2g} Raman peak of ceria.

Acknowledgment

Universiti Brunei Darussalam (Grant No. UBD-ORI-URC-RG331-U01 and UBD/OVACRI/CRGWG(004)/170101), and Ministry of Science and Technology of Taiwan (MOST 106-2112-M-019-005-MY3). We also would like to thank Prof. Hai-Pang Chiang from Institute of Optoelectronic Sciences, National Taiwan Ocean University, Keelung 202, Taiwan, for his assistance with the Raman measurement.

References

[1] L. Minervini, M.O. Zacate, and R.W. Grimes, "Defect cluster formation in M_2O_3-doped CeO_2," Solid State Ionics, vol. 116, Jan. 1999, pp. 339-349, doi: https://doi.org/10.1016/S0167-2738(98)00359-2.

[2] A. Walsh, S.M. Woodley, C.R.A. Catlow, and A.A. Sokol, "Potential energy landscapes for anion Frenkel-pair formation in ceria and india," Solid State Ionics, vol. 184, Mar. 2011, pp. 52-56, doi: https://doi.org/10.1016/j.ssi.2010.08.010.

[3] T.X.T. Sayle, M. Molinari, S. Das, U.M. Bhatta, G. Möbus, S.C. Parker, S. Seal, and D.C. Sayle, "Environment-mediated structure, surface redox activity and reactivity of ceria nanoparticles," Nanoscale, vol. 5, May 2013, pp. 6063-6073, doi: https://doi.org/10.1039/C3NR00917C.

[4] E. Mamontov, T. Egami, R. Brezny, M. Koranne, and S. Tyagi, "Lattice Defects and Oxygen

Storage Capacity of Nanocrystalline Ceria and Ceria-Zirconia," The Journal of Physical Chemistry B, vol. 104, Oct. 2000, pp. 11110-11116, doi: https://doi.org/10.1021/jp0023011.

[5] H. He, H.X. Dai, and C.T. Au, "Defective structure, oxygen mobility, oxygen storage capacity, and redox properties of RE-based (RE = Ce, Pr) solid solutions," Catalysis Today, vol. 90, July 2004, pp. 245-254, doi: https://doi.org/10.1016/j.cattod.2004.04.033.

[6] K. Sudarshan, S.K. Sharma, R. Gupta, S.K. Gupta, F.N. Sayed, and P.K. Pujari, "Role of surface defects in catalytic properties of CeO_2 nanoparticles towards oxygen reduction reaction," Materials Chemistry and Physics, vol. 200, Oct. 2017, pp. 99-106, doi: https://doi.org/10.1016/j.matchemphys.2017.07.064.

[7] J.A. Rodriguez, S. Ma, P. Liu, J. Hrbek, J. Evans, and M. Pérez, "Activity of CeO_x and TiO_x nanoparticles grown on Au(111) in the water-gas shift reaction," Science, vol. 318, Dec. 2007, pp. 1757-1760, doi: https://doi.org/10.1126/science.1150038.

[8] J. Shi, A. Schaefer, A. Wichmann, M.M. Murshed, T.M. Gesing, A. Wittstock, and M. Bäumer, "Nanoporous gold-supported ceria for the water–gas shift reaction: UHV Inspired Design for Applied Catalysis," The Journal of Physical Chemistry C, vol. 118, July 2014, pp. 29270-29277, doi: https://doi.org/10.1021/jp505433a.

[9] M. Molinari, S.C. Parker, D.C. Sayle, and M.S. Islam, "Water adsorption and its effect on the stability of low index stoichiometric and reduced surfaces of ceria," The Journal of Physical Chemistry C, vol. 116, Feb. 2012, pp. 7073-7082, doi: https://doi.org/ 10.1021/jp300576b.

[10] S. Gangopadhyay, D.D. Frolov, A.E. Masunov, and S. Seal, "Structure and properties of cerium oxides in bulk and nanoparticulate forms," Journal of Alloys and Compounds, vol. 584, Jan. 2014, pp. 199-208, doi: https://doi.org/10.1016/j.jallcom.2013.09.013.

[11] H. Muta, H. Kado, Y. Ohishi, K. Kurosaki, and S. Yamanaka, "Effect of oxygen defects on thermal conductivity of thorium-cerium dioxide solid solutions," Journal of Nuclear Materials, vol. 483, Jan. 2017, pp. 192-198, doi: https://doi.org/10.1016/j.jnucmat.2016.10.043.

[12] M. Wilklow-Marnell, and W.D. Jones, "Catalytic oxidation of carbon monoxide by α-alumina supported 3nm cerium dioxide nanoparticles," Molecular Catalysis, vol. 439, Oct. 2017, pp. 9-14, doi: https://doi.org/10.1016/j.mcat.2017.06.015.

[13] M. Lohrenscheit, and C. Hess, "Direct evidence for the participation of oxygen vacancies in the oxidation of carbon monoxide over ceria-supported gold catalysts by using operando Raman spectroscopy," ChemCatChem, vol. 8, Feb. 2016, pp. 523-526, doi: https://doi.org/10.1002/cctc.201501129.

[14] T. Taniguchi, T. Watanabe, N. Sugiyama, A.K. Subramani, H. Wagata, N. Matsushita, and M. Yoshimura, "Identifying defects in ceria-based nanocrystals by UV resonance Raman spectroscopy," The Journal of Physical Chemistry C, vol. 113, Oct. 2009, pp. 19789-19793, doi: https://doi.org/10.1021/jp9049457.

[15] Z. Wu, M. Li, J. Howe, H.M. Meyer III, and S.H. Overbury, "Probing defect sites on CeO_2 nanocrystals with well-defined surface planes by Raman spectroscopy and O_2 adsorption," Langmuir, vol. 26, July 2010, pp. 16595-16606, doi: https://doi.org/10.1021/la101723w.

[16] S. Agarwal, X. Zhu, E.J.M. Hensen, L. Lefferts, and B.L. Mojet, "Defect chemistry of ceria nanorods," The Journal of Physical Chemistry C, vol. 118, Feb. 2014, pp. 4131-4142, doi: https://doi.org/10.1021/jp409989y.

[17] Y.F. Chou Chau, C.M. Lim, C. Lee, H.J. Huang, C.T. Lin, N.T.R.N. Kumara, V.N. Yoong, and H.P. Chiang, "Tailoring surface plasmon resonance and dipole cavity plasmon modes of scattering cross section spectra on the single solid-gold/gold-shell nanorod," Journal of Applied Physics, vol. 120, Sept. 2016, pp. 093110, doi: https://doi.org/10.1063/1.4962175.

[18] M.W. Chen, Y.F. Chau, and D.P. Tsai, "Three-dimensional analysis of scattering field interactions and surface plasmon resonance in coupled silver nanospheres," Plasmonics, vol. 3, Dec. 2008, pp. 157-164, doi: https://doi.org/10.1007/s11468-008-9069-8.

[19] Y.F. Chau, and Z.H. Jiang, "Plasmonics effects of nanometal embedded in a dielectric

substrate," Plasmonics, vol. 6, Sept. 2011, pp. 581-589, doi: https://doi.org/10.1007/s11468-011-9238-z.

[20] K.Y. Yang, Y.F. Chau, Y.W. Huang, H.Y. Yeh, and D.P. Tsai, "Design of high birefringence and low confinement loss photonic crystal fibers with five rings hexagonal and octagonal symmetry air-holes in fiber cladding," Journal of Applied Physics, vol. 109, May 2011, pp. 093103, doi: https://doi.org/10.1063/1.3583560.

[21] M.G. Sanchez, and J.L. Gazquez, "Oxygen vacancy model in strong metal-support interaction," Journal of Catalysis, vol. 104, Mar. 1987, pp. 120-135, doi: https://doi.org/10.1016/0021-9517(87)90342-3.

[22] W.Y. Hernández, F. Romero-Sarria, M.A. Centeno, and J.A. Odriozola, "In situ characterization of the dynamic gold−support interaction over ceria modified Eu3+. Influence of the oxygen vacancies on the CO oxidation reaction," The Journal of Physical Chemistry C, vol. 114, Jun. 2010, pp. 10857-10865, doi: https://doi.org/10.1021/jp1013225.

[23] S. Bhagat, N.V.S. Vallabani, V. Shutthanandan, M. Bowden, A.S. Karakoti, and S. Singh, "Gold core/ceria shell-based redox active nanozyme mimicking the biological multienzyme complex phenomenon," Journal of Colloid and Interface Science, vol. 513, Mar. 2018, pp. 831-842, doi: https://doi.org/10.1016/j.jcis.2017.11.064.

[24] Y. Lee, G. He, A.J. Akey, R. Si, M. Flytzani-Stephanopoulos, and I.P. Herman, "Raman analysis of mode softening in nanoparticle $CeO_{2-\delta}$ and Au-$CeO_{2-\delta}$ during CO oxidation," Journal of the American Chemical Society, vol. 133, July 2011, pp. 12952-12955, doi: https://doi.org/10.1021/ja204479j.

[25] K. Sambasivudu, Y.B. Reddy, J.S. Yadav, G. Sabitha, and D. Shailaja, "Ceria-supported vinylpyridine polymers: synthesis, characterization and application in catalysis," International Journal of Polymeric Materials and Polymeric Biomaterials, vol. 57, July 2008, pp. 891-903, doi: https://doi.org/10.1080/00914030802153199.

[26] W.H. Weber, K.C. Hass, and J.R. McBride, "Raman study of CeO_2: Second-order scattering, lattice dynamics, and particle-size effects," Physical Review B, vol. 48, July 1993, pp. 178-185, doi: https://doi.org/10.1103/PhysRevB.48.178.

[27] J.E. Spanier, R.D. Robinson, F. Zhang, S.W. Chan, and I.P. Herman, "Size-dependent properties of CeO_{2-y} nanoparticles as studied by Raman scanttering," Physical Review B, vol. 64, Nov. 2001, pp. 245407, doi: https://doi.org/10.1103/PhysRevB.64.245407.

[28] Z.V. Popović, Z. Dohčević-Mitrović, M. Šćepanović, M. Grujić-Brojčin, and S. Aškrabić, "Raman scattering on nanomaterials and nanostructures," Annalen der Physik, vol. 523, Jan. 2011, pp. 62-74, doi: https://doi.org/10.1002/andp.201000094.

[29] Z.V. Popović, Z. Dohčević-Mitrović, A. Cros, and A. Cantarero, "Raman scattering study of the anharmonic effects in CeO_{2-y} nanocrystals," Journal of Physics: Condensed Matter, vol. 19, Nov. 2007, pp. 496209, doi: https://doi.org/10.1088/0953-8984/19/49/496209.

[30] J.R. Adleman, D.A. Boyd, D.G. Goodwin, and D. Psaltis, "Heterogenous catalysis mediated by plasmon heating," Nano Letters, vol. 9, Nov. 2009, pp. 4417-4423, doi: https://doi.org/10.1021/nl902711n.

[31] P. B. Johnson, and R. W. Christy, "Optical constants of the noble metals," Physical Review B, vol. 6, Dec. 1972, pp. 4370-4379, doi: https://doi.org/10.1103/PhysRevB.6.4370.

[32] Y.F. Chau, Z.H. Jiang, H.Y. Li, G.M. Lin, F.L. Wu, and W.H. Lin, "Localized resonance of composite core-shell nanospheres, nanobars and nanospherical chains," Progress In Electromagnetics Research B, vol. 28, 2011, pp. 183-199, doi: https://doi.org/10.2528/PIERB10102705.

[33] Y.F. Chau, H.H. Yeh, and D.P. Tsai, "Surface plasmon resonances effects on different patterns of solid-silver and silver-shell nanocylindrical pairs," Journal of Electromagnetic Waves and Applications, vol. 24, 2010, pp. 1005-1014, doi: https://doi.org/10.1163/156939310791586098.

[34] Y.F. Chau, and H.H. Yeh, "A comparative study of solid-silver and silver-shell nanodimers on

surface plasmon resonances," Journal of Nanoparticle Research, vol. 13, Feb. 2011, pp. 637-644, doi: https://doi.org/10.1007/s11051-010-0058-4.

[35] Y.F. Chau, "Surface plasmon effects excited by the dielectric hole in a silver-shell nanospherical pair," Plasmonics, vol. 4, Dec. 2009, pp. 253, doi: https://doi.org/10.1007/s11468-009-9100-8.